Journal of Materials Chemistry A

ROYAL SOCIETY OF CHEMISTRY

PAPER

View Article Online
View Journal

Cite this: DOI: 10.1039/d5ta08347h

Regenerable oxygen-deficient Ni/γ-Al_2O_3 catalyst for efficient glycerol aqueous phase reforming†

Jung Hyun Park, [a] Hong Lu, [a] Brajendra K. Sharma, [b] David Johnston,[b] Nandakishore Rajagopalan[a] and Jaemin Kim *[a]

Aqueous phase reforming (APR) of glycerol represents a promising pathway for sustainable fuel gas generation. Nickel-immobilized gamma alumina (Ni/γ-Al_2O_3) has been recognized as an effective alternative to noble metal catalysts, but the phase transformation from γ-Al_2O_3 to AlOOH under hydrothermal conditions negatively affects its long-term catalytic performance. To address this challenge, we synthesized a Ni/γ-Al_2O_3 catalyst *via* a Ni-exsolution technique from $NiAl_2O_4$ spinel oxide. The catalyst achieved a gasification yield of 49.2% with a fuel gas energy of 9.2 MJ kg^{-1} of glycerol in 45 min at 250 °C, producing hydrogen, carbon monoxide, and methane, which is comparable to that of the Ru-catalyst. The spent catalyst was regenerated, resulting in an increased gasification yield of 52.6% and fuel gas energy of 10.3 MJ kg^{-1} of glycerol, with enhanced H_2 (106.7%) and CH_4 (123.0%) production compared to the fresh catalyst. This remarkable performance is primarily attributed to improved crystallinity of γ-Al_2O_3 and strengthened Ni and γ-Al_2O_3 interactions induced by increased oxygen vacancies and electron density. This study highlights the significance of the metal exsolution approach in catalyst preparation, demonstrating that chemical structure modulation through regeneration is crucial for enhancing both the catalytic activity and durability of γ-Al_2O_3 supported catalysts in glycerol APR.

Received 13th October 2025
Accepted 2nd December 2025

DOI: 10.1039/d5ta08347h

rsc.li/materials-a

Introduction

Producing fuel gases such as hydrogen (H_2) and methane (CH_4) from sustainable feedstock is key to developing cleaner energy routes. Glycerol, a renewable byproduct from biodiesel manufacturing[1–3] and bioethanol production,[4–7] is an attractive feedstock for the aqueous phase reforming (APR) process due to its oversupply relative to demand. The APR of glycerol produces carbon monoxide (CO) and H_2 (eqn (1)), while the produced CO is most likely converted to carbon dioxide (CO_2) and H_2 *via* the water–gas shift (WGS) reaction (eqn (2)). Overall, APR of glycerol is described by using eqn (3):[8]

$$C_3H_8O_3\ (l) \rightarrow 3CO + 4H_2\ \Delta H^\circ = 245\ kJ\ mol^{-1} \quad (1)$$

$$CO + H_2O \leftrightarrow CO_2 + H_2\ \Delta H^\circ = -41\ kJ\ mol^{-1} \quad (2)$$

$$C_3H_8O_3\ (l) + 3H_2O \leftrightarrow 7H_2 + 3CO_2\ \Delta H^\circ = 123\ kJ\ mol^{-1} \quad (3)$$

The produced CO, CO_2, and H_2 can be further converted to methane through reactions in eqn (4) and (5), respectively:

$$CO + 3H_2 \leftrightarrow CH_4 + H_2O\ \Delta H^\circ = -206\ kJ\ mol^{-1} \quad (4)$$

$$CO_2 + 4H_2 \leftrightarrow CH_4 + 2H_2O\ \Delta H^\circ = -165\ kJ\ mol^{-1} \quad (5)$$

Fuel gas yields are strongly influenced by the catalyst used under typical APR reaction conditions (~250 °C; ~580 psig).[9–12] For practical applications, catalysts must exhibit excellent hydrothermal stability to sustain fuel gas production over time. The desired catalyst possesses uniform dispersion of active metals, small particle size, strong metal–support interactions, and highly exposed triple-phase boundaries among the catalyst, support, and reactants.[13] In this context, careful selection of catalyst materials with tailored synthesis methods is crucial for developing durable, practical catalysts for sustainable fuel gas production.

Nickel-based catalysts are attractive alternatives to noble metal-based catalysts such as Ru, Pd, and Pt in biomass treatment due to their earth abundance and excellent catalytic performance. Nickel as a catalytic center is active for C–C bond cleavage, water–gas shift, and methanation reactions.[14] In addition to Ni, metal oxide supports such as Al_2O_3, ZrO_2, and CeO_2 can enhance the catalytic performance of Ni by modulating the electronic structure and dispersing Ni nanoparticles to optimize active site exposure.[15,16] γ-Al_2O_3 features a porous structure with abundant acidic and basic sites that facilitate

[a]*Illinois Sustainable Technology Center, University of Illinois at Urbana-Champaign, 1Hazelwood Drive, Champaign, IL 61820, USA. E-mail: jaemin@illinois.edu*

[b]*U.S. Department of Agriculture, Agricultural Research Service, Eastern Regional Research Center, Sustainable Biofuels and Co-Products Research Unit, 600 E. Mermaid Lane, Wyndmoor, PA 19038, USA*

† Mention of trade names or commercial products in this article is solely for the purpose of providing specific information and does not imply recommendation or endorsement by the U.S. Department of Agriculture. USDA is an equal opportunity provider and employer.

catalytic reactions through strong interaction with reactants.[17,18] Therefore, Ni supported on γ-Al_2O_3 (Ni/γ-Al_2O_3) has been extensively studied for hydrothermal biomass treatment[16,19–21] and methanation processes.[22–25] γ-Al_2O_3, however, suffers from low hydrothermal stability, which undergoes phase transformation to AlOOH, leading to structural collapse and activity loss.[26–28] Nonetheless, effective strategies to improve the hydrothermal stability of γ-Al_2O_3 without compromising catalytic performance remain scarce, making this an ongoing research challenge.[29]

Metal exsolution techniques, unlike conventional catalyst reduction, enable the formation of homogeneously dispersed, finely anchored metal nanoparticles on an oxide support,[30–33] leading to exceptional catalytic activity.[34–36] Additionally, oxygen vacancies within the oxide lattice serve as crucial active sites that promote water activation and enhance CO_2 chemisorption.[37–39] Here, we present a Ni/γ-Al_2O_3 catalyst, prepared by exsolving Ni from $NiAl_2O_4$ spinel oxide, for producing fuel gases from glycerol APR (Scheme 1). The Ni/γ-Al_2O_3 catalyst, characterized by uniformly distributed Ni nanoparticles on a γ-Al_2O_3 support, demonstrated high yields of H_2, CO, and CH_4 in glycerol APR. We carefully investigated the catalytic pathways and active sites using X-ray photoelectron spectroscopy (XPS) and proton nuclear magnetic resonance (^{1}H-NMR), and examined the phase segregation process during APR. The spent, phase-segregated catalysts were regenerated through consecutive calcination and exsolution processes, which presented enhanced catalytic activity with improved hydrothermal stability. Comprehensive XPS characterization confirmed that increased oxygen vacancies and enhanced γ-Al_2O_3 crystallinity significantly contributed to the improved catalytic activity and stability in glycerol APR.

Results and discussion

Synthesis of Ni/γ-Al_2O_3 through Ni-exsolution

Ni/γ-Al_2O_3 was prepared *via* Ni-exsolution from $NiAl_2O_4$ spinel oxide. The initial Ni–Al complex was prepared by a sol–gel method using $Ni(NO_3)_2 \cdot 6H_2O$ and $Al(NO_3)_3 \cdot 9H_2O$ as metal precursors and citric acid as a chelating agent. $NiAl_2O_4$ spinel was obtained through calcination of the Ni–Al complex at 800 °C for 6 h in an air environment. The scanning electron microscope (SEM) image in Fig. S1a supports that as-prepared $NiAl_2O_4$ has irregular morphology with relatively large, undefined particles. A higher-magnification SEM image in Fig. 1a further confirmed the smooth surface feature of $NiAl_2O_4$. After the exsolution process, Ni/γ-Al_2O_3 exhibited well-dispersed Ni nanoparticles (Ni NPs, 20–30 nm) anchored on the support surface, while its overall morphology remained largely unchanged (Fig. 1b and S1b).

The structure of $NiAl_2O_4$ and Ni/γ-Al_2O_3 was further investigated using X-ray diffraction (XRD) spectroscopy, as shown in Fig. 1c. The diffraction patterns of the prepared $NiAl_2O_4$

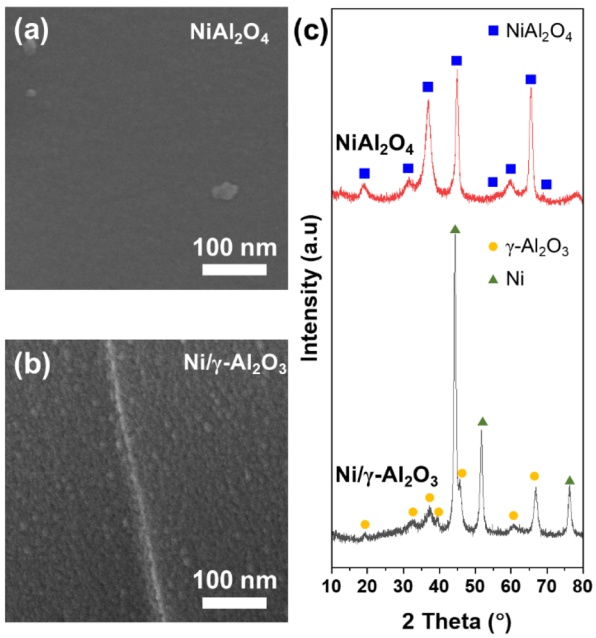

Fig. 1 Characterization of the prepared compounds. SEM images of (a) $NiAl_2O_4$ spinel oxide and (b) the Ni/γ-Al_2O_3 catalyst. (c) X-ray diffraction patterns before ($NiAl_2O_4$) and after reduction (Ni/γ-Al_2O_3).

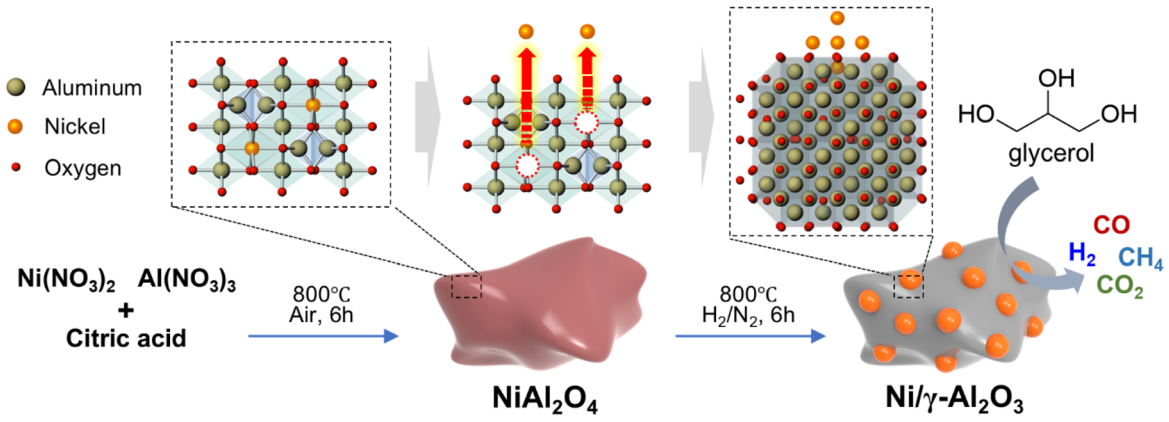

Scheme 1 Illustration depicting the exsolution of Ni nanoparticles from $NiAl_2O_4$ spinel oxide to generate the Ni/γ-Al_2O_3 catalyst for enhanced aqueous phase reforming (APR) of glycerol.

matched well with the reference peaks of $NiAl_2O_4$ (PDF# 01-078-6956), with the *Fd*-3*ms* space group and cubic crystal structure. Exsolved Ni NPs from the parent $NiAl_2O_4$ spinel were clearly observed from the XRD patterns after the reduction process, while characteristic peaks for $NiAl_2O_4$ were not detected. Well-developed diffraction peaks at 2θ degrees of 44.4, 51.7, and 76.3 correspond to the (111), (200), and (220) facets, respectively, of cubic structured *Fm*-3*m* Ni (PDF# 01-076-4179). The Ni NP size was calculated to be 25.7 nm using the Scherrer equation, which is in good agreement with the particle size observed in the SEM images (Fig. 1b). The rest of the diffraction peaks are matched with γ-phase Al_2O_3 (PDF# 01-076-4179), whose space group is *Fd*-3*mZ* with a cubic crystal structure. These suggest the successful exsolution of Ni NPs from $NiAl_2O_4$ with complete phase transformation. The structure of the Ni-exsolved catalyst was examined at various temperatures, indicating that 800 °C is the minimum temperature required to fully convert $NiAl_2O_4$ into Ni/γ-Al_2O_3 (Fig. S2). This finding is consistent with the hydrogen temperature-programmed reduction (H_2-TPR) results reported in previous literature,[40] which indicated complete reduction of Ni species near this temperature.

For controls, Ni NPs and Ni/γ-Al_2O_3 were additionally prepared by the hydrothermal process and conventional wet impregnation method, respectively. Ni nanoparticles prepared *via* the hydrothermal process had a spherical shape with wide particle size distribution in the 100–300 nm range (Fig. S3 and S4). Ni/γ-Al_2O_3, prepared by the conventional wet impregnation (Ni/γ-Al_2O_3_w) method, presented Ni nanoparticle sizes from 40 to 110 nm on γ-Al_2O_3, resulting from the uncontrollable Ni agglomeration at the reduction step (Fig. S5 and S6). It is noteworthy that, unlike Ni/γ-Al_2O_3_w, Ni NPs in Ni/γ-Al_2O_3 are strongly anchored on the surface of γ-Al_2O_3,[41] resulting in a homogeneous particle size distribution (20–30 nm). The uniform dispersion of Ni NPs provides a high density of accessible Ni active sites and triple-phase boundaries, which are essential for efficient glycerol APR and methanation reactions.

APR of glycerol

The glycerol APR was conducted in a Parr high-pressure reactor using 1.0 g of the Ni/γ-Al_2O_3 catalyst and 30 mL of a 0.2 M glycerol aqueous solution at 250 °C. The evolution of gaseous products (H_2, CO, CH_4, and CO_2) was monitored every 15 min for 45 min (Fig. 2). In Ni/γ-Al_2O_3-catalyzed APR, 12 mmol H_2 and 1.9 mmol CO were produced within the first 15 min (Fig. 2a and b). Then H_2 production yield remained largely unchanged for 45 min whereas CO decreased to <0.5 mmol. In the meantime, CH_4 production gradually increased and reached a maximum yield of 1.3 mmol at 45 min (Fig. 2c). The observed CH_4 formation is likely attributed to the methanation reactions of CO and CO_2 with H_2, where the γ-Al_2O_3 support facilitates the chemisorption of CO and CO_2 (Fig. 2d).[42–45]

The gasification yield of glycerol is presented in Fig. 2e. The yield was determined by a carbon balance calculation, comparing the total carbon in the glycerol feed with the carbon detected in the gaseous products, CO, CH_4, and CO_2. The gasification yield reached 49.2% at 45 min. The observed yield is comparable to that of Ru catalysts,[46,47] which is attributed to the

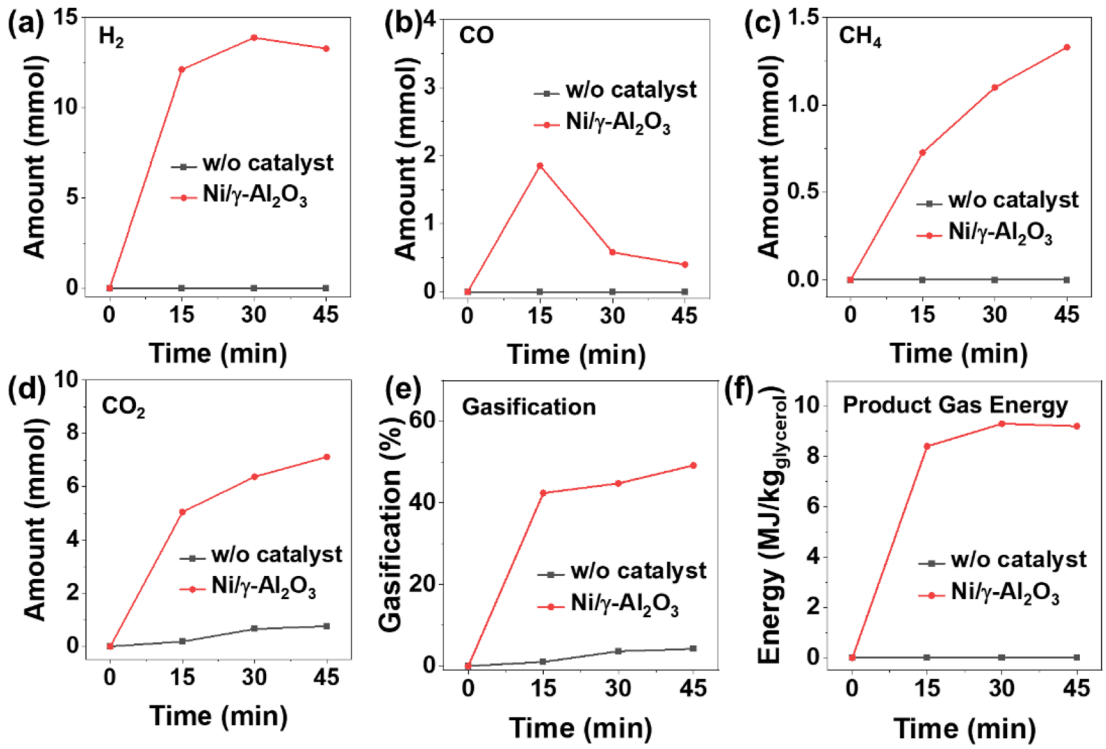

Fig. 2 The catalytic performance of the Ni/γ-Al_2O_3 catalyst for APR of glycerol at 250 °C. The production of (a) hydrogen, (b) carbon monoxide, (c) methane, and (d) carbon dioxide. (e) Gasification yield of glycerol and (f) energy of the gas products as a function of time.

increased triple phase boundaries surrounding Ni NPs achieved through the metal exsolution approach. To further evaluate the fuel quality, the energy of the product gas was determined (Fig. 2f). The gas product energy was stabilized at 9.2 MJ kg^{-1} of glycerol after 30 min and remained unchanged for an additional 15 min. The higher heating value (HHV) of the gas product obtained under the Ni/γ-Al_2O_3 system was calculated to be 13.7 MJ kg^{-1} (Table S1).

The catalytic performance of Ni/γ-Al_2O_3 was evaluated with control catalysts, Ni NPs, γ-Al_2O_3, and Ni/γ-Al_2O_3_w, in at least three independent experiments, as shown in Fig. 3. In the tests, Ni NPs produced on average 8.7 mmol H_2, 0.5 mmol CO, 0.8 mmol CH_4, and 6.9 mmol CO_2. The gasification yield of Ni NPs was 45.8%, which was similar to that of Ni/γ-Al_2O_3 (49.2%). However, Ni/γ-Al_2O_3 produced 52.1% more H_2 and 62.2% more CH_4, despite containing only 35.5% Ni content by chemical composition. These results indicate that the enhanced H_2 and CH_4 production of Ni/γ-Al_2O_3 is mainly attributed to the increased chemisorption of CO and CO_2 on the γ-Al_2O_3 support.[42,45] γ-Al_2O_3 alone, in contrast, showed negligible catalytic activity for glycerol APR, producing minimal amounts of H_2 (0.08 mmol), CO (0.02 mmol), CH_4 (0.04 mmol), and CO_2 (1.2 mmol), comparable to the non-catalyzed system (H_2: 0 mmol, CO: 0 mmol, CH_4: 0 mmol, and CO_2: 0.8 mmol). The gasification yield of γ-Al_2O_3 alone was only 6.8%, confirming that active metallic Ni NPs are the primary catalytic sites and γ-Al_2O_3 mainly serves for chemisorption of CO and CO_2 rather than direct fuel gas production. For the Ni/γ-Al_2O_3_w control catalyst, the average gasification yield was 31.1%, most likely due to reduced active sites and triple phase boundaries resulting from the larger Ni particle size (40–110 nm) compared to that of Ni/γ-Al_2O_3 (20–30 nm). The HHV for the gas product, which was influenced by the relative proportion of the combustible gases, was evaluated to be 9.7, 1.2 and 13 MJ kg^{-1} in the presence of Ni NPs, γ-Al_2O_3, and Ni/γ-Al_2O_3_w, respectively (Table S1). Overall, the performed control experiments highlight the significance of the Ni exsolution strategy for APR catalysts, which generates smaller, uniformly dispersed Ni nanoparticles on the support.

Ni/γ-Al_2O_3 was further tested in a pure water system, in the absence of glycerol, to elucidate the origin of hydrogen and carbon in fuel gas production. The measured gas products were 1.5 mmol H_2, 1.1 mmol CO_2, and a negligible amount of CH_4 (0.03 mmol). This result indicates that Ni/γ-Al_2O_3 can activate water to produce H_2. Taken together with the negligible H_2 production observed from the γ-Al_2O_3 system, it is evident that Ni NPs play a crucial role in H_2 evolution from water. The low CH_4 yield is likely attributed to dissolved CO_2 in water, as reflected in the CO_2 production from the γ-Al_2O_3 system. $NiAl_2O_4$ was also tested for the glycerol APR, where 10.4 mmol of H_2 and 2.2 mmol of CO_2 were produced with negligible CO and CH_4 generation and a low gasification yield of 13.7% (Fig. S7).

Glycerol APR reaction pathways

To investigate the glycerol APR reaction pathway in the Ni/γ-Al_2O_3 system, individual reaction tests were conducted using γ-Al_2O_3, Ni NPs, and Ni/γ-Al_2O_3 catalysts, respectively. The intermediate species generated from each reaction were characterized using nuclear magnetic resonance (NMR) spectroscopy (Fig. S8–S11 and 4). The APR of glycerol has been understood to proceed primarily through two pathways:[48] (1) a dehydration

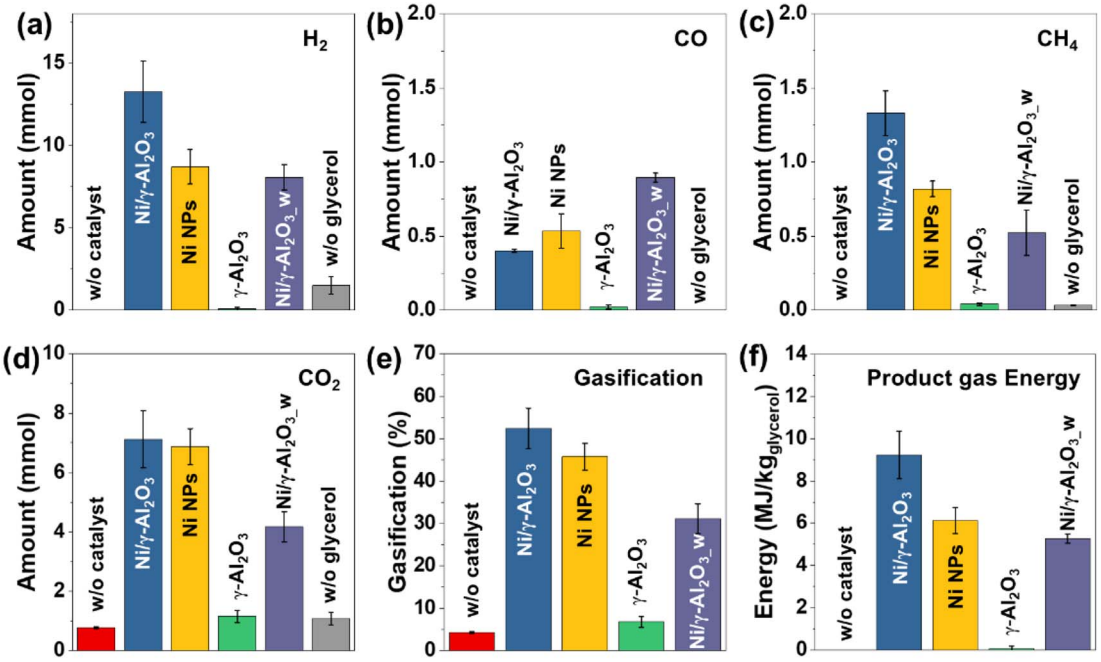

Fig. 3 Control experiments for APR of glycerol at 250 °C under an N_2 atmosphere. Comparison of gas productions: (a) hydrogen, (b) carbon monoxide, (c) methane, and (d) carbon dioxide. (e) Gasification yields on a carbon basis and (f) energy of the gas products. All experiments were conducted at least three times to ensure reproducibility.

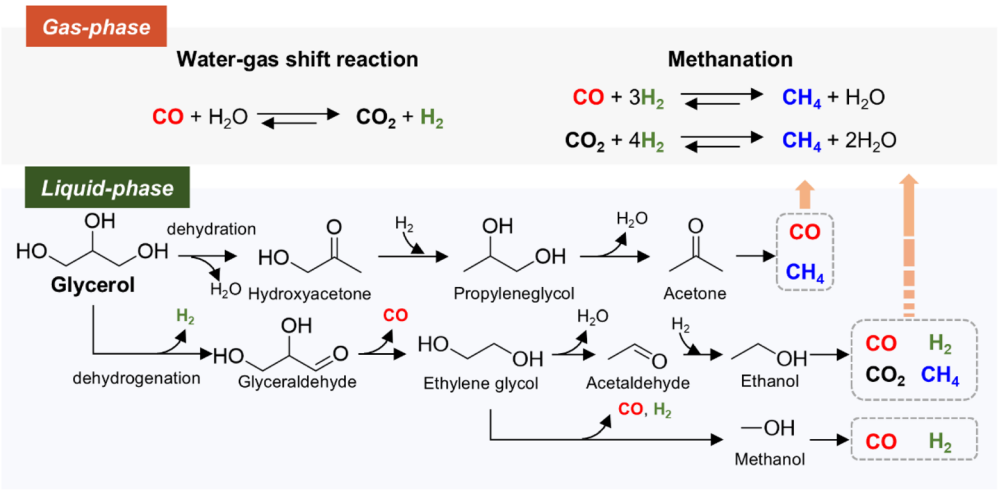

Fig. 4 Suggested reaction mechanisms for the APR of glycerol over the Ni/γ-Al_2O_3 catalyst at 250 °C under a N_2 atmosphere.

pathway yielding hydroxyacetone as an intermediate and (2) a dehydrogenation pathway yielding glyceraldehyde as an intermediate.

In the glycerol APR test using γ-Al_2O_3 alone, the ^{1}H-NMR spectrum exhibited a multiplet at 3.78 ppm along with two doublets of doublet at 3.65 ppm and 3.55 ppm, corresponding to the characteristic proton peaks for glycerol (Fig. S8). This observation aligns with the negligible gasification yield shown in Fig. 3e. Hydroxyacetone (singlets at 4.37 ppm and 2.14 ppm) and propyleneglycol (doublet of doublet at 3.43 ppm and doublet at 1.13 ppm) were detected, indicating that the dehydration pathway is dominant in the presence of γ-Al_2O_3.[36,48] Ethanol was identified by a triplet at 1.18 ppm, whereas the expected quartet at 3.65 ppm was not resolved due to overlap with the glycerol peak. The trace ethanol likely results in minor CO production (Fig. 3b), which is produced alongside hydrogen.[40,48] This hydrogen is possibly utilized for the hydrogenation of hydroxyacetone to propyleneglycol, with the remaining H_2 detected in Fig. 3a.

In the Ni NP-catalyzed glycerol APR system, glycerol was rarely detected, while weak peaks attributed to acetaldehyde appeared at 9.67 ppm (quartet) and 2.24 ppm (doublet) (Fig. S9). Relatively intense peaks corresponding to ethanol (triplet at 1.18 ppm; quartet at 3.65 ppm) and acetone (singlet at 2.23 ppm) further indicate that both dehydration and dehydrogenation pathways are active. However, considering the high H_2 and CO production yields in Fig. 3a and b, it can be inferred that the dehydrogenation pathway is predominant, as glyceraldehyde formation produces more H_2 and CO than hydroxyacetone.[48,49]

In the presence of Ni/γ-Al_2O_3, glycerol APR reaction solutions were analyzed at 30 min and 45 min. The ^{1}H-NMR spectra of the 30 min sample (Fig. S10) presented a distinct quartet peak at 9.67 ppm along with an intense doublet at 2.24 ppm for acetaldehyde. In addition, a quartet at 5.25 ppm and a doublet at 1.32 ppm correspond to ethane-1,1′-diol, likely formed *via* hydration of acetaldehyde.[50,51] The simultaneous presence of Ni NPs and γ-Al_2O_3 facilitates glycerol conversion to both hydroxyacetone and glyceraldehyde.[40] Since Ni/γ-Al_2O_3 actively produces H_2 from glycerol and water (Fig. 3a), sufficient hydrogen is available to hydrogenate hydroxyacetone to propyleneglycol. This intermediate subsequently dehydrates to acetone (2.23 ppm, singlet), which can further generate CO and CH_4. In 45 min (Fig. S11), most of the hydroxyacetone, propyleneglycol, and acetone were consumed. The observed decrease in ethanol and methanol (singlet at 3.36 ppm) further supports the predominance of the dehydrogenation pathway, consistent with increased CO, H_2, and CO_2 production.

Overall, Ni/γ-Al_2O_3 converts glycerol into both hydroxyacetone and glyceraldehyde *via* dehydration and dehydrogenation pathways, respectively, leading to the formation of H_2, CO, CH_4, and CO_2. These gaseous products undergo water–gas shift and methanation reactions on the catalyst surface, resulting in fuel gas production. The strong chemisorption of CO_2 and CO on γ-Al_2O_3, combined with the increased triple phase boundaries in Ni/γ-Al_2O_3, underpins its excellent catalytic activity for fuel gas generation. Although acetic acid and 2-propanol are potential intermediates in glycerol APR, they were not detected in the reaction mixture of this study.

Catalyst stability and regeneration

To evaluate the durability of the Ni/γ-Al_2O_3 catalyst, the spent catalyst was recovered after glycerol APR and subsequently characterized. XRD analysis in Fig. 5a showed that the majority of γ-Al_2O_3 was converted into AlOOH (PDF# 01-073-9093) with an orthorhombic crystal structure (*Cmcm* space group) during the reaction. Notably, the characteristic reflections of γ-Al_2O_3 were completely absent after the reaction, indicating a thorough phase conversion. Only a weak diffraction peak for γ-Al_2O_3 was observed at a 2θ degree of 45.8, in line with previous reports that γ-Al_2O_3 hydrates to form AlOOH under aqueous phase conditions.[26–28] XRD peaks for metallic Ni became more prominent after glycerol APR without further oxidation into NiO_x. The SEM image of the used catalyst showed a reduction in

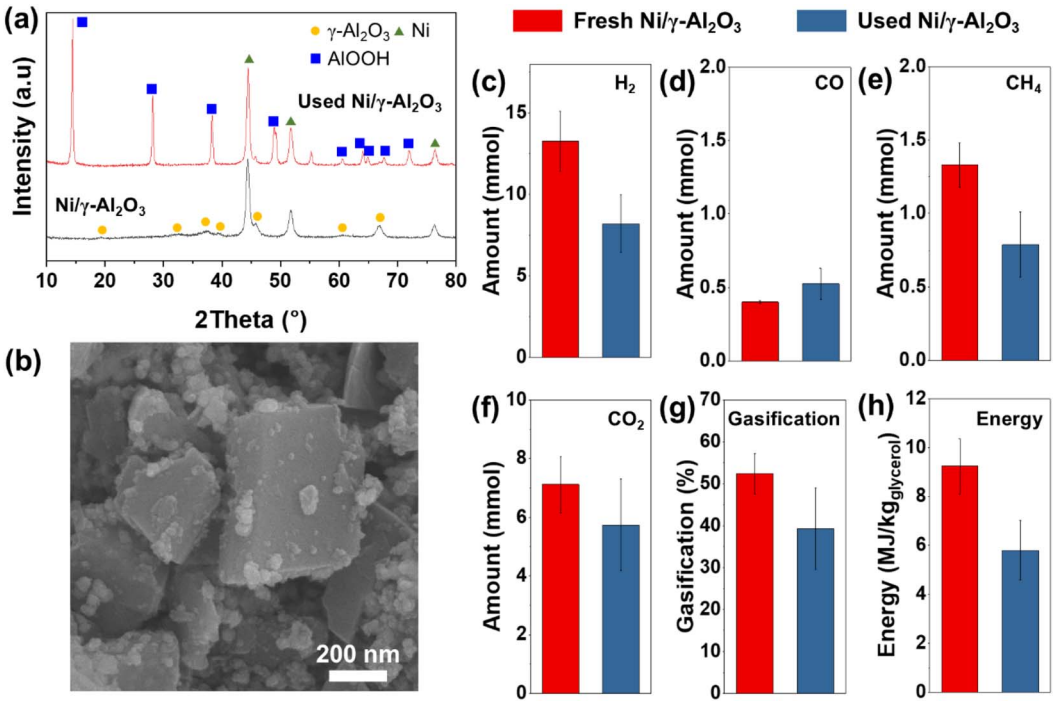

Fig. 5 Catalytic performance of the used Ni/γ-Al_2O_3 catalyst. (a) XRD patterns and (b) SEM image of the used Ni/γ-Al_2O_3 catalyst. Comparison of fresh Ni/γ-Al_2O_3 and used Ni/γ-Al_2O_3 catalysts: (c) hydrogen, (d) carbon monoxide, (e) methane, and (f) carbon dioxide production. (g) Gasification yields of glycerol on a carbon basis and (h) HHV of the gas products. At least three independent experiments were conducted to ensure reliability.

particle size as a result of the phase transition from γ-Al_2O_3 to AlOOH (Fig. S12). While agglomeration of Ni NPs was observed due to the instability of the support, some Ni NPs remained anchored, retaining their original particle size, as shown in Fig. 5b.

The spent Ni/γ-Al_2O_3 catalyst was reused for glycerol APR to clarify the catalytically active species (Fig. 5c–h). Upon reuse, the catalyst produced 8.2 mmol H_2, 0.52 mmol CO, 0.79 mmol CH_4, and 5.7 mmol CO_2, resulting in a decreased gasification yield of 39.3% and product gas energy of 5.8 MJ kg^{-1} of glycerol. This result closely resembled that of Ni NPs or Ni/γ-Al_2O_3_w (Fig. 3). Given the smaller Ni particle size observed on the used catalyst compared to the fresh Ni NPs and Ni/γ-Al_2O_3_w, it is likely that the catalytic activity originated primarily from the Ni NPs present in the used catalyst. These results indicate that the catalyst exhibits excellent activity when Ni is strongly bound to γ-Al_2O_3 rather than AlOOH, thereby emphasizing the importance of restoring the Ni/γ-Al_2O_3 structure to maintain optimal catalytic performance.

To extend the lifetime of the spent catalyst by regeneration, the used Ni/γ-Al_2O_3 was collected by centrifugation and subjected to sequential treatments as shown in Fig. 6a. The used catalyst was first calcined at 800 °C for 6 h in air to form $NiAl_2O_4$ spinel oxide (Regen. $NiAl_2O_4$). It is worth noting that Ni/γ-Al_2O_3 prepared by the conventional wet impregnation method can partially be converted to $NiAl_2O_4$ under similar conditions, but the entire phase transformation has not been reported,[26,52,53] and the conversion of Ni/AlOOH to $NiAl_2O_4$ remains unexplored. We have previously demonstrated a similar regeneration strategy for catalysts prepared *via* the metal exsolution technique.[34] The converted phase after calcination was characterized by XRD (Fig. 6b). Notably, the peak at a 2θ degree of 37.3 became more intense, which can be attributed to the overlap between the $NiAl_2O_4$ spinel phase and the (111) facet of newly formed NiO. Additionally, XRD peaks at 2θ degrees of 43.3, 62.9, 75.44, and 79.4 correspond to the (111), (200), (220), (311), and (222) facets of NiO, respectively, confirming the presence of residual NiO in the regenerated $NiAl_2O_4$. The presence of NiO peaks suggests incomplete incorporation of Ni into the $NiAl_2O_4$ lattice, which may result from agglomeration of Ni NPs during the conversion of Al_2O_3 to AlOOH in the APR process.

The Regen. $NiAl_2O_4$ was further reduced at 800 °C for 6 h under a 10% H_2 atmosphere to re-form Ni/γ-Al_2O_3, and its structure was characterized in Fig. 6c. The resulting diffraction patterns closely matched those of the fresh Ni/γ-Al_2O_3, while sharper Ni peaks were observed after the regeneration process. Notably, the peaks corresponding to γ-Al_2O_3 at 2θ degrees of 37.3, 39.3 and 45.6 became more pronounced, indicating increased crystallinity of the γ-Al_2O_3 support after regeneration. This improved crystallinity is likely to contribute to enhanced hydrothermal stability of γ-Al_2O_3 under APR conditions, which will be discussed further in a later section.

The SEM image in Fig. 6d shows a well-defined structure of the Regen. $NiAl_2O_4$, with particle sizes comparable to those of the used catalyst, ranging from hundreds of nanometers to micrometers (Fig. S12). Smaller particles observed in Regen.

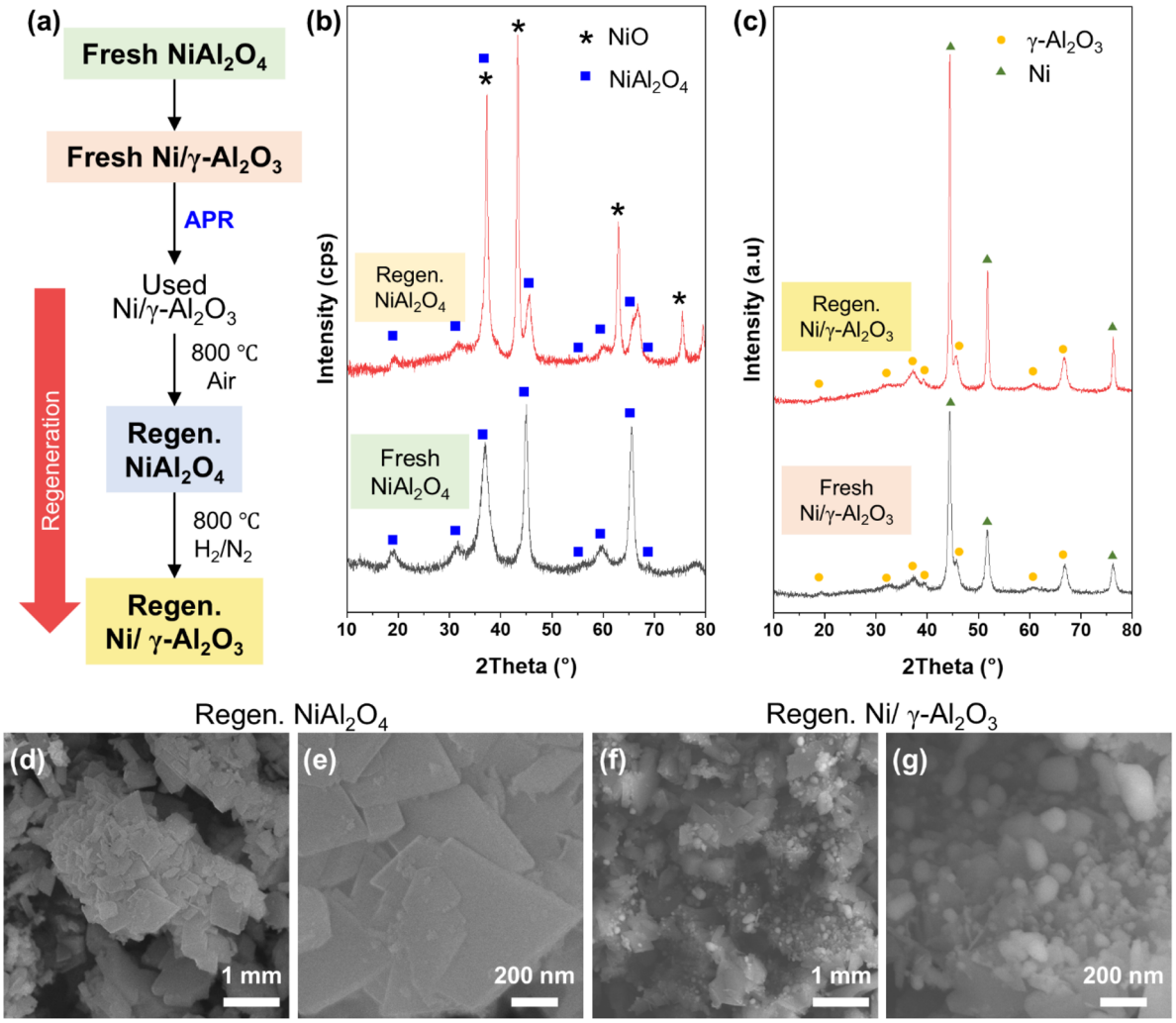

Fig. 6 (a) Sequential regeneration route of the used Ni/γ-Al_2O_3 catalyst and XRD spectral comparison of (b) fresh and regenerated $NiAl_2O_4$ spinel oxides and (c) fresh and regenerated Ni/γ-Al_2O_3 catalysts. SEM images of (d) and (e) regenerated $NiAl_2O_4$ spinel oxide and (f) and (g) regenerated Ni/γ-Al_2O_3.

$NiAl_2O_4$ in Fig. 6e are NiO particles, as confirmed by XRD data. The overall morphology of the Regen. $NiAl_2O_4$ was retained during the reduction process to produce Regen. Ni/γ-Al_2O_3, resulting in numerous exsolved Ni NPs on the γ-Al_2O_3 surface (Fig. 6f and g). Energy dispersive X-ray spectroscopy (EDS) mapping presented that the larger, well-defined particles predominantly consist of Al and O, while the smaller particles are Ni NPs (Fig. S13), indicating agglomeration and a less uniform Ni distribution compared to the fresh Ni/γ-Al_2O_3 catalyst. This agglomeration likely arises from the presence of large NiO particles formed on the spinel oxide during regeneration.

To evaluate the influence of AlOOH and NiO on particle size and morphology during regeneration, fresh Ni/γ-Al_2O_3 was further regenerated without conducting the APR process (Regen. $NiAl_2O_4$ w/o APR) for comparison. The XRD patterns of Regen. $NiAl_2O_4$ w/o APR displayed less pronounced NiO peaks (2θ degrees of 43.3, 62.9, 75.44, and 79.4) compared to Regen. $NiAl_2O_4$ that was regenerated after the glycerol APR process (Fig. S14). This difference implies that the absence of phase transformation from γ-Al_2O_3 to AlOOH provides better anchoring, and less agglomeration and formation of NiO. Consequently, the regenerated Ni/γ-Al_2O_3 without the glycerol APR process (Regen. Ni/γ-Al_2O_3 w/o APR) exhibited a more intense Ni diffraction peak (2θ degrees of 44.4, 51.7, and 76.3), which correlates with the increased Ni NP size observed in SEM images (Fig. S15). Detailed glycerol APR performance using the Regen. Ni/γ-Al_2O_3 w/o APR catalyst will be shown and discussed in a later section.

The catalytic performance of Regen. Ni/γ-Al_2O_3 is presented in Fig. 7. Regen. Ni/γ-Al_2O_3 produced 14.2 mmol H_2, 0.8 mmol CO, 1.6 mmol CH_4, and 7.0 mmol CO_2, which are comparable to or higher than those of the fresh Ni/γ-Al_2O_3 catalyst. It showed a high gasification yield of 52.6% with a product gas energy of 10.3 MJ kg^{-1} of glycerol and HHV of 14.8 MJ kg^{-1}. This higher fuel gas energy, compared to the fresh catalyst (9.2 MJ kg^{-1} of glycerol), is mainly attributed to the increased fuel gas production of H_2 (106.7%) and CH_4 (123%), despite the Regen.

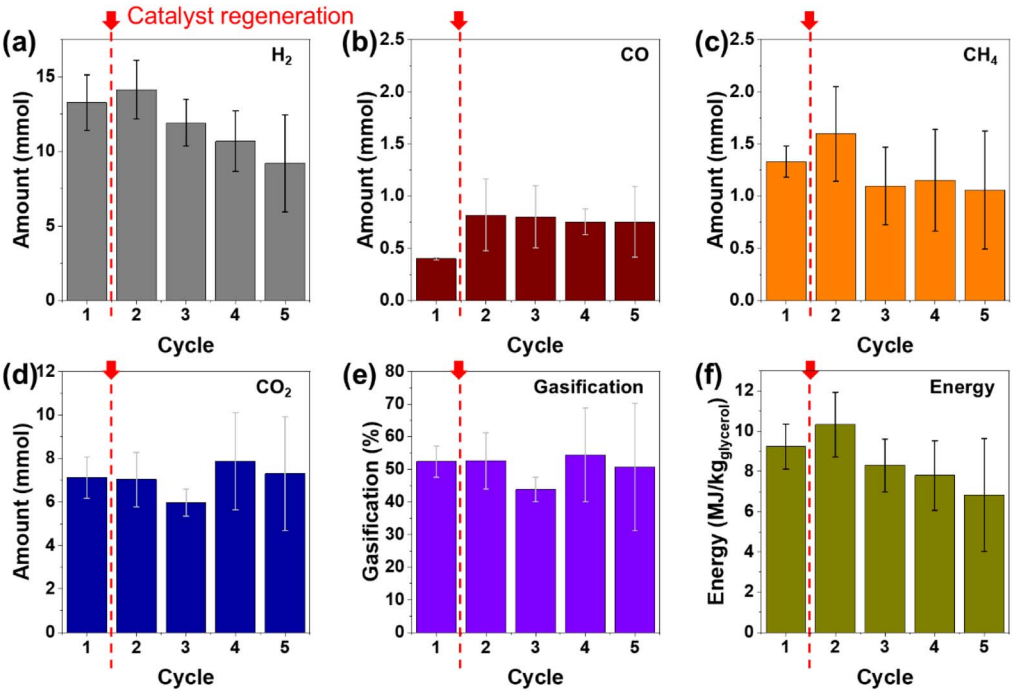

Fig. 7 Glycerol APR performance of the regenerated Ni/γ-Al_2O_3 catalyst. The amounts of gas products: (a) hydrogen, (b) carbon monoxide, (c) methane, and (d) carbon dioxide. (e) Gasification yield of glycerol on a carbon basis, and (f) HHV of the gas products. An arrow (red) indicates the regeneration process.

Ni/γ-Al_2O_3 catalyst containing larger Ni NPs with fewer exposed triple-phase boundaries.

The improved hydrothermal stability of the Regen. Ni/γ-Al_2O_3 catalyst was observed through consecutive cyclic tests (cycles 3–5 in Fig. 7) conducted without further regeneration: H_2 production gradually decreased to 9.2 mmol by the 5th cycle, whereas CO and CH_4 yields remained stable at 0.8 mmol and 1.1 mmol, respectively. XRD analysis for the cyclic tests (Fig. S16) further confirmed the enhanced stability of the Regen. Ni/γ-Al_2O_3 catalyst. The catalyst exhibited only minor structural

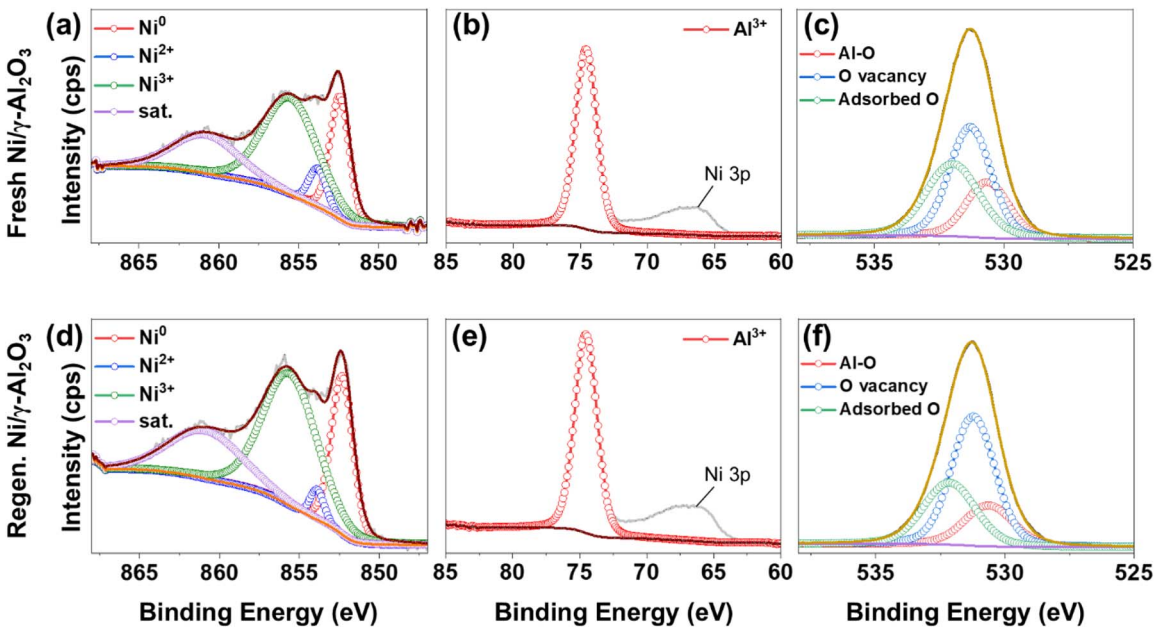

Fig. 8 XPS spectra of fresh and regenerated Ni/γ-Al_2O_3. (a) Ni 2p, (b) Al 2p, and (c) O 1s spectra of fresh Ni/γ-Al_2O_3, and (d) Ni 2p, (e) Al 2p, and (f) O 1s spectra of regenerated Ni/γ-Al_2O_3.

Table 1 XPS analysis results of fresh and regenerated Ni/γ-Al_2O_3

		Nickel				Oxygen		
		Ni^0	Ni^{2+}	Ni^{3+}	Aluminum	Al–O	O_v	O_{ad}
Fresh Ni/γ-Al_2O_3	Binding energy [eV]	852.4	853.8	855.5	74.5	530.6	531.3	532.0
	Amount [%]	28.9	8.3	62.8		21.9	42.5	35.7
Regen. Ni/γ-Al_2O_3	Binding energy [eV]	852.3	853.9	855.6	74.6	530.6	531.2	532.1
	Amount [%]	31.6	3.8	64.6		18.4	51.9	29.7

changes over the cycles, which is in great contrast to the fresh Ni/γ-Al_2O_3 that underwent complete transformation into Ni/AlOOH (Fig. 5a). The diffraction peaks of Regen. γ-Al_2O_3 remained largely unchanged with increased γ-Al_2O_3 crystallinity, although peaks corresponding to AlOOH gradually appeared during repeated glycerol APR cycles. Overall, the regenerated catalyst, Regen. Ni/γ-Al_2O_3, demonstrated improved hydrothermal stability and sustained catalytic performance compared to the fresh catalyst.

The catalytic activity of Regen. Ni/γ-Al_2O_3 w/o APR was further evaluated as shown in Fig. S17. Despite possessing smaller Ni NPs and a greater exposure of triple phase boundaries than Regen. Ni/γ-Al_2O_3, the catalyst exhibited lower activity in glycerol APR by producing 9.6 mmol H_2, 0.5 mmol CO, 1.0 mmol CH_4, and 5.1 mmol CO_2 with a HHV of 6.8 MJ kg^{-1} of glycerol. These results importantly indicate that the phase transformation from γ-Al_2O_3 to AlOOH not only promotes Ni NP agglomeration but also alters the catalyst's chemical structure in ways that critically impact its catalytic activity for glycerol APR.

To examine the correlation between glycerol APR performance (activity and durability) and the chemical structure of the catalysts, X-ray photoelectron spectroscopy (XPS) was performed on fresh Ni/γ-Al_2O_3, Regen. Ni/γ-Al_2O_3, and Regen. Ni/γ-Al_2O_3 w/o APR (Fig. 8 and S19). All spectra were deconvoluted using the C–C bond from the C 1s peak at 284.8 eV as a reference (Fig. S18) as the initial step for analysis. In the Ni 2p XPS spectrum of the fresh Ni/γ-Al_2O_3 catalyst (Fig. 8a), metallic Ni (Ni^0) was identified at 852.4 eV, while peaks for Ni^{2+} and Ni^{3+} appeared at 853.8 and 855.5 eV, respectively. The Al 2p XPS spectrum (Fig. 8b) shows a peak at 74.5 eV corresponding to Al^{3+}, and a characteristic peak of γ-Al_2O_3, with an additional peak at 70–65 eV attributed to the Ni 3p orbital. The O 1s XPS spectrum in Fig. 8c shows lattice oxygen (Al–O) at 530.6 eV, an oxygen vacancy at 531.3 eV, and adsorbed oxygen at 532.0 eV.[54–57]

For Regen. Ni/γ-Al_2O_3, notable shifts and changes were observed in all three spectra. The Ni^0 peak in the Ni 2p spectrum shifted by 0.1 eV to lower binding energy (852.3 eV), indicating enhanced electron density, and the proportion of Ni^0 increased from 28.9 to 31.6% (Fig. 8d). As metallic Ni serves as the active site, its increased content strongly correlates with improved catalytic performance.[58–60] In contrast, Ni^{2+} and Ni^{3+} peaks shifted by 0.1 eV to higher binding energy, which is attributed to the strengthened interactions between the support and exsolved Ni NPs. Similarly, the Al 2p peak in the regenerated catalyst shifted by 0.1 eV to higher binding energy (Fig. 8e). Considering the increased crystallinity observed in XRD data (Fig. 6c), this shift suggests stronger interactions between Ni and γ-Al_2O_3, while improved support crystallinity contributes to enhanced hydrothermal stability.

Oxygen vacancies, recognized as active sites for water activation and CO/CO_2 chemisorption,[61] showed a significant increase for Regen. Ni/γ-Al_2O_3. In the O 1s XPS spectrum (Fig. 8f), the lattice oxygen peak remained unchanged, while the oxygen vacancy peak shifted from 531.3 to 531.2 eV, and the adsorbed oxygen peak shifted from 532.0 to 532.1 eV, indicating the increased relative concentration of oxygen vacancies. The calculated oxygen vacancy content increased from 42.5% to 51.9%. XPS data suggest that the increased amounts of metallic Ni and oxygen vacancies in Regen. Ni/γ-Al_2O_3 likely contributed to its sustained and robust catalytic performance, despite the presence of larger Ni NPs and fewer exposed triple phase boundaries.[35,62]

The origin of the oxygen vacancy was examined by comparing XPS data of Regen. $NiAl_2O_4$ and Regen. Ni/γ-Al_2O_3 w/o APR (Fig. S19–S21 and Table S2). The regenerated $NiAl_2O_4$ spinel oxide exhibited increased oxygen vacancies, estimated at 51.6% based on the relative area of the vacancy-associated peak in the O 1s spectrum, compared to 39.0% in the fresh $NiAl_2O_4$. Consequently, Regen. $NiAl_2O_4$ showed a lower Ni^{2+} binding energy of 853.3 eV, compared to 853.9 eV in fresh $NiAl_2O_4$, consistent with the lower binding energy of metals in oxygen-deficient metal oxides.[38,62–64] This confirms the presence of increased oxygen vacant sites in Regen. Ni/γ-Al_2O_3. In contrast, Regen. Ni/γ-Al_2O_3 w/o APR exhibited a similar level of oxygen vacancy content (42.4%) to that of fresh Ni/γ-Al_2O_3. In summary, the phase transformation (γ-Al_2O_3 → AlOOH → γ-Al_2O_3) during regeneration is crucial to generate abundant oxygen vacancies in the γ-Al_2O_3 support while enhancing its crystallinity as evidenced by a 0.3 eV shift in the Al^{3+} peak (from 74.2 eV to 74.5 eV). Together, these changes contributed to the improved catalytic activity and durability of the Regen Ni/γ-Al_2O_3 catalyst. The detailed XPS peak deconvolution and quantitative results are summarized in Table 1, providing a comparative overview of the electronic states and elemental compositions for fresh and regenerated catalysts.

Conclusions

In this study, we demonstrated the enhanced catalytic performance of the Ni/γ-Al_2O_3 catalyst for fuel gas production *via* glycerol APR. The Ni/γ-Al_2O_3 catalyst was prepared using a Ni-

exsolution technique starting from $NiAl_2O_4$ spinel oxide as the parent material. With homogeneously distributed Ni nanoparticles, the catalyst exhibited excellent activity towards H_2, CO, and CH_4 production under mild reaction conditions. Mechanistic analysis revealed that the Ni/γ-Al_2O_3 catalyst promotes both dehydration and dehydrogenation pathways during glycerol conversion to gaseous products. To assess durability, the spent catalyst was regenerated through sequential heat treatments. The regenerated catalyst (Regen. Ni/γ-Al_2O_3) showed improved catalytic activity and durability in consecutive cyclic tests. These enhancements are mainly attributed to the increased crystallinity of the oxide support and strengthened interactions between Ni and γ-Al_2O_3, facilitated by increased oxygen vacancies and electron density, as confirmed by XPS analysis. Overall, these findings not only advance the understanding of glycerol APR, but also create new opportunities to enhance the catalytic activity and stability of γ-Al_2O_3-supported catalysts for diverse aqueous phase reactions and sustainable fuel gas production from various biomass-derived waste streams, thereby promoting integrated waste-to-fuel strategies within circular bioeconomy frameworks.

Experimental

Materials

All chemicals were used without further purification. Nickel nitrate hexahydrate (98%), aluminum nitrate nonahydrate (98%), hydrazine hydrate solution (>98.0%), γ-Al_2O_3 (99.95%), and sodium hydroxide (98%) were purchased from Sigma-Aldrich (USA). Citric acid (99%), nickel chloride hexahydrate (99.3%), and glycerol (99%) were purchased from Fisher Scientific (USA).

Synthesis of the Ni/γ-Al_2O_3 catalyst

$NiAl_2O_4$ spinel oxide was prepared *via* a sol–gel process using citric acid as the chelating agent. In a typical preparation, 2.9 g (10 mmol) of $Ni(NO_3)_2\cdot 6H_2O$, 7.5 g (20 mmol) of $Al(NO_3)_3\cdot 9H_2O$, and 12.6 g (60 mmol) of citric acid were dissolved in 50 mL of deionized water in a 200 mL beaker under continuous stirring. The solution was heated at 150 °C overnight, yielding a dried solid complex. The resulting product was ground into a fine powder using a mortar and pestle and subsequently calcined in air at 800 °C for 6 h with a ramping rate of 5 °C min^{-1} to produce $NiAl_2O_4$. Finally, the $NiAl_2O_4$ powder was reduced under 10% H_2 (90% N_2) at 800 °C for 6 h leading to exsolution of Ni nanoparticles on γ-Al_2O_3 (denoted as Ni/γ-Al_2O_3).

As a control, Ni/γ-Al_2O_3 was also prepared *via* a conventional wet impregnation method. 8.43 g (20 mmol) of $Ni(NO_3)_2\cdot 6H_2O$ was dissolved in 100 mL of methanol and 2 g (20 mmol) of γ-Al_2O_3 powder was added. The suspension was stirred at 80 °C overnight to ensure uniform adsorption of the nickel precursor onto the support. The resulting dry powder was collected and reduced under 10% H_2 (90% N_2) at 800 °C for 6 h to yield Ni nanoparticle immobilized γ-Al_2O_3 (denoted as Ni/γ-Al_2O_3_w).

Synthesis of Ni nanoparticles

For Ni nanoparticle preparation, 4 g of NaOH and 2 g of $NiCl_2\cdot 6H_2O$ were dissolved in 32 mL and 20 mL of an ethanol–water mixture (2 : 1 v/v), respectively. These solutions were then mixed, and 10 mL of hydrazine monohydrate was added dropwise. The mixture was transferred to a Teflon-lined autoclave (200 mL) and heated at 115 °C for 2 h. The product was washed three times using water and ethanol, respectively, followed by centrifugation at 8000 rpm.

APR of glycerol

The as-prepared Ni/γ-Al2O3 catalyst (1 g) and 30 mL of 0.2 M glycerol solution were added to a 250 mL Parr reactor (Series 4570 HP/HT reactor, Parr Instrument Company, USA) equipped with a reactor controller (Model: 4848, Parr Instrument Company, USA). The reactor was sealed, evaluated for leakage using 400 psig of nitrogen gas, and purged with 400 psig of nitrogen six times. The reactor was heated to 250 °C for about 50 min, and the glycerol hydrothermal treatment was conducted. The measured pressure at 250 °C was 600 psig. Gas samples from the headspace of the reactor were collected by water substitution and analyzed by using a thermal conductivity detector (TCD)-equipped gas chromatograph (GC, 5890 Series II, Hewlett Packard, USA) using helium as a carrier gas. Calibration of the instrument was achieved using standard reference gases of ultra-high purity grade, and the volume change during the hydrothermal gasification was compensated by measuring the N_2 concentration in the headspace of the reactor. The gasification yield was calculated using eqn (6):

$$\text{G.Y.} = \frac{M_{CO} + M_{CH_4} + M_{CO_2}}{M_{C,glycerol}} \times 100(\%) \quad (6)$$

where G.Y. is the gasification yield of glycerol in aqueous phase reforming under subcritical water conditions, M_{CO}, MC_{H_4}, and M_{CO_2} are molar amounts of CO, CH_4, and CO_2 obtained after the reaction, and $M_{C,glycerol}$ is the molar amount of carbon in the glycerol solution. The quantification of H_2 includes generation from both glycerol and water.

The higher heating value (HHV) of the fuel gases produced from glycerol was calculated using the following equation:

$$\text{HHV} = -\sum_i m_i \times \Delta_c H_i^{\circ} \quad (7)$$

where HHV is the higher heating value of the fuel gas produced from glycerol (MJ kg^{-1}), i is a compound in the product fuel gas, m is the mass of the compound in the fuel gas (kg kg^{-1}), and $\Delta_c H^{\circ}$ is the standard heat of combustion (MJ kg^{-1}).

Regeneration of the spent catalyst

The spent catalyst was collected by using a centrifuge at 8000 rpm for 10 min and was rinsed using water and ethanol three times. Then the used catalyst was heated at 800 °C for 6 h with a ramping rate of 5 °C min^{-1} in an air atmosphere. The resulting $NiAl_2O_4$ spinel (denoted as Regen. $NiAl_2O_4$) was further reduced by a thermal treatment at 800 °C for 6 h with

a ramping rate of 5 °C min^{-1} under 10% H_2 (90% N_2) to obtain regenerated Ni/γ-Al_2O_3 (denoted as Regen. Ni/γ-Al_2O_3).

Author contributions

Jung Hyun Park: conceptualization, methodology, data curation, writing – original draft, visualization, investigation. Hong Lu: methodology, writing – review & editing. Brajendra Kumar Sharma: writing – review & editing. David Johnston: writing – review & editing. Nandakishore Rajagopalan: writing – review & editing, supervision. Jaemin Kim: funding acquisition, conceptualization, writing – review & editing, supervision.

Conflicts of interest

There are no conflicts to declare.

Data availability

The data supporting this article have been included as part of the supplementary information (SI). Supplementary information is available. See DOI: https://doi.org/10.1039/d5ta08347h.

Acknowledgements

This work was supported by the USDA Agriculture and Food Research Initiative (AFRI), project award no. 2024-67021-42492, from the U.S. Department of Agriculture's National Institute of Food and Agriculture. Powder XRD was performed in George L. Clark X-Ray Facility and 3M Materials Laboratory in School of Chemical Sciences (SCS) at the University of Illinois, Urbana-Champaign (UIUC). The NMR study was carried out in the NMR laboratory in SCS at UIUC. SEM and XPS were carried out in Materials Research Laboratory (MRL) Central Facilities at UIUC.

References

1 C. Venu, D. Palanisamy, S. Jaganathan and S. Rajendran, *Renew. Energy*, 2023, **219**, 119594.
2 F. Yang, M. A. Hanna and R. Sun, *Biotechnol. Biofuels*, 2012, **5**, 13.
3 S. Haosagul, N. Vikromvarasiri, V. Sawasdee and N. Pisutpaisal, *Int. J. Hydrogen Energy*, 2019, **44**, 29568–29574.
4 Y. Kim, N. S. Mosier, R. Hendrickson, T. Ezeji, H. Blaschek, B. Dien, M. Cotta, B. Dale and M. R. Ladisch, *Bioresour. Technol.*, 2008, **99**, 5165–5176.
5 K. Liu, *J. Agr. Food Chem.*, 2011, **59**, 1508–1526.
6 F. Adom, J. Fan, J. Davis, P. Dunn and D. Shonnard, *ACS Sustain. Chem. Eng.*, 2014, **2**, 1139–1146.
7 K. Ratanapariyanuch, Y. Y. Shim, S. Emami and M. J. T. Reaney, *J. Agr. Food Chem.*, 2016, **64**, 9488–9496.
8 N. A. Roslan, S. Z. Abidin, A. Ideris and D.-V. N. Vo, *Int. J. Hydrogen Energy*, 2020, **45**, 18466–18489.
9 S. Leng, S. Barghi and C. Xu, *npj Mater. Sustain.*, 2024, **2**, 19.
10 L. Santiago-Martínez, M. Li, P. Munoz-Briones, J. Vergara-Zambrano, S. Avraamidou, J. A. Dumesic and G. W. Huber, *Green Chem.*, 2024, **26**, 7212–7230.
11 F. Bastan, M. Kazemeini and A. S. Larimi, *Renew. Energy*, 2017, **108**, 417–424.
12 A. Iriondo, V. L. Barrio, J. F. Cambra, P. L. Arias, M. B. Güemez, R. M. Navarro, M. C. Sánchez-Sánchez and J. L. G. Fierro, *Top. Catal.*, 2008, **49**, 46–58.
13 J. Oh, S. Joo, C. Lim, H. J. Kim, F. Ciucci, J.-Q. Wang, J. W. Han and G. Kim, *Angew. Chem., Int. Ed.*, 2022, **61**, e202204990.
14 R. R. Davda, J. W. Shabaker, G. W. Huber, R. D. Cortright and J. A. Dumesic, *Appl. Catal., B*, 2003, **43**, 13–26.
15 J. Li, Y. Tu, K. He, C. Chen, L. Liang, C. Ruan and Q. Zhang, *Molecules*, 2025, **30**, 1310.
16 P. Azadi, E. Afif, F. Azadi and R. Farnood, *Green Chem.*, 2012, **14**, 1766–1777.
17 S. Carré, N. S. Gnep, R. Revel and P. Magnoux, in *Studies in Surface Science and Catalysis*, ed. A. Gédéon, P. Massiani and F. Babonneau, Elsevier, 2008, vol. 174, pp. 973–976.
18 H. Knozinger, in *Studies in Surface Science and Catalysis*, ed. B. Imelik, C. Naccache, G. Coudurier, Y. B. Taarit and J. C. Vedrine, Elsevier, 1985, vol. 20, pp. 111–125.
19 F. Bastan and M. Kazemeini, *Biomass Convers. Bior.*, 2023, **13**, 237–246.
20 M. M. Rahman, T. L. Church, A. I. Minett and A. T. Harris, *ChemSusChem*, 2013, **6**, 1006–1013.
21 M. Z. Hossain, M. R. Karim, S. Sutradhar, M. B. I. Chowdhury and P. A. Charpentier, *Int. J. Hydrogen Energy*, 2023, **48**, 39791–39804.
22 S. Abelló, C. Berrueco and D. Montané, *Fuel*, 2013, **113**, 598–609.
23 J. Kumar Prabhakar, P. A. Apte and G. Deo, *Chem.–Eng. J.*, 2023, **471**, 144252.
24 G. Garbarino, C. Wang, T. Cavattoni, E. Finocchio, P. Riani, M. Flytzani-Stephanopoulos and G. Busca, *Appl. Catal., B*, 2019, **248**, 286–297.
25 G. Garbarino, P. Kowalik, P. Riani, K. Antoniak-Jurak, P. Pieta, A. Lewalska-Graczyk, W. Lisowski, R. Nowakowski, G. Busca and I. S. Pieta, *Ind. Eng. Chem. Res.*, 2021, **60**, 6554–6564.
26 R. S. Zhou and R. L. Snyder, *Acta Cryst.*, 1991, **47**, 617–630.
27 X. Liang, J. Tang, L. Li and Y. Wu, *JOM*, 2023, **75**, 4689–4700.
28 A. P. Amrute, K. Jeske, Z. Łodziana, G. Prieto and F. Schüth, *Chem. Mater.*, 2020, **32**, 4369–4374.
29 Y. Zhang, B. Huang, M. K. Mardkhe and B. F. Woodfield, *Microporous Mesoporous Mater.*, 2019, **284**, 60–68.
30 J. Mei, T. Liao and Z. Sun, *Mater. Today Energy*, 2023, **31**, 101216.
31 M. L. Weber, B. Šmíd, U. Breuer, M.-A. Rose, N. H. Menzler, R. Dittmann, R. Waser, O. Guillon, F. Gunkel and C. Lenser, *Nat. Mater.*, 2024, **23**, 406–413.
32 A. Bonkowski, M. J. Wolf, J. Wu, S. C. Parker, A. Klein and R. A. De Souza, *J. Am. Chem. Soc.*, 2024, **146**, 23012–23021.
33 D. Neagu, T.-S. Oh, D. N. Miller, H. Ménard, S. M. Bukhari, S. R. Gamble, R. J. Gorte, J. M. Vohs and J. T. S. Irvine, *Nat. Commun.*, 2015, **6**, 8120.

34 J. H. Park, J. W. Scott, H. Lu, N. Rajagopalan, B. K. Sharma, S. D. Cosper, K. J. Hay and J. Kim, *Chem.–Eng. J.*, 2024, **486**, 150330.
35 A. Kumar, D. R. Kanchan, A. Banerjee, B. P. Singh and R. Srivastava, *ACS Catal.*, 2025, **15**, 8239–8258.
36 M. Shokrollahi Yancheshmeh, O. Alizadeh Sahraei, M. Aissaoui and M. C. Iliuta, *Appl. Catal., B*, 2020, **265**, 118535.
37 S. Zhao, Y. Wen, C. Du, T. Tang and D. Kang, *Chem.–Eng. J.*, 2020, **402**, 126180.
38 T. Zhang, W. Wang, F. Gu, W. Xu, J. Zhang, Z. Li, T. Zhu, G. Xu, Z. Zhong and F. Su, *Appl. Catal., B*, 2022, **312**, 121385.
39 H. Fu and H. Lian, *Chem.–Eng. J.*, 2024, **489**, 151021.
40 A. Morales-Marín, J. L. Ayastuy, U. Iriarte-Velasco and M. A. Gutiérrez-Ortiz, *Appl. Catal., B*, 2019, **244**, 931–945.
41 O. Kwon, S. Joo, S. Choi, S. Sengodan and G. Kim, *J. Phys. Energy*, 2020, **2**, 032001.
42 K. Föttinger, W. Emhofer, D. Lennon and G. Rupprechter, *Top. Catal.*, 2017, **60**, 1722–1734.
43 S.-n. Yin, J. Zhao, S. Wu, X. Han and J. Ren, *Chem.–Eng. J.*, 2025, **504**, 158723.
44 Y. Li, C. Shen, C. Jiang, C. Liang, B. Chen, W. Ding and X. Guo, *ACS Catal.*, 2025, **15**, 9728–9737.
45 S. Liu, Z. Zhou, J. Chen, Y. Fu and C. Cai, *Appl. Surf. Sci.*, 2023, **611**, 155645.
46 S. Jeon, Y. M. Park, J. Park, K. Saravanan, H.-K. Jeong and J. W. Bae, *Appl. Catal., A*, 2018, **551**, 49–62.
47 P. Gogoi, A. S. Nagpure, P. Kandasamy, C. V. V. Satyanarayana and T. Raja, *Sustain. Energy Fuels*, 2020, **4**, 678–690.
48 A. Fasolini, D. Cespi, T. Tabanelli, R. Cucciniello and F. Cavani, *Catalysis*, 2019, **9**, 722.
49 B. C. M. Morales and B. A. O. Quesada, *Catal. Today*, 2021, **372**, 115–125.
50 G. Socrates, *J. Org. Chem.*, 1969, **34**, 2958–2961.
51 P. Diederich, T. Geisberger, Y. Yan, C. Seitz, A. Ruf, C. Huber, N. Hertkorn and P. Schmitt-Kopplin, *Commun. Chem.*, 2023, **6**, 38.
52 M. A. Goula, N. D. Charisiou, K. N. Papageridis, A. Delimitis, E. Pachatouridou and E. F. Iliopoulou, *Int. J. Hydrogen Energy*, 2015, **40**, 9183–9200.
53 G. Garbarino, C. Wang, I. Valsamakis, S. Chitsazan, P. Riani, E. Finocchio, M. Flytzani-Stephanopoulos and G. Busca, *Appl. Catal., B*, 2015, **174–175**, 21–34.
54 D. Li, Y. Li, X. Liu, Y. Guo, C.-W. Pao, J.-L. Chen, Y. Hu and Y. Wang, *ACS Catal.*, 2019, **9**, 9671–9682.
55 G. Caravaggio, L. Nossova and M. J. Turnbull, *Chem.–Eng. J.*, 2021, **405**, 126862.
56 M. Han, Z. Wang, Y. Xu, R. Wu, S. Jiao, Y. Chen and S. Feng, *Mater. Chem. Phys.*, 2018, **215**, 251–258.
57 J. Wang, D. N. Mueller and E. J. Crumlin, *J. Eur. Ceram. Soc.*, 2024, **44**, 116709.
58 Z. Refaat, M. E. Saied, A. O. A. E. Naga, S. A. Shaban, H. B. Hassan, M. R. Shehata and F. Y. E. Kady, *Sci. Rep.*, 2023, **13**, 4855.
59 Y. Kong, X. Jia, X. Chai, Z. Chen, C. Shang, X. Jiang, H. Cai, L. Jing, Q. Hu, H. Yang, X. Zhang and C. He, *Natl. Sci. Rev.*, 2025, **12**, nwaf173.
60 L. Shen, J. Xu, M. Zhu and Y.-F. Han, *ACS Catal.*, 2020, **10**, 14581–14591.
61 Z. Wei, M. Zhao, Z. Yang, X. Duan, G. Jiang, G. Li, F. Zhang and Z. Hao, *Proc. Natl. Acad. Sci. U. S. A.*, 2023, **120**, e2217148120.
62 G. S. More, B. P. Singh, R. Bal and R. Srivastava, *Inorg. Chem.*, 2023, **62**, 13069–13080.
63 B. Bharti, S. Kumar, H.-N. Lee and R. Kumar, *Sci. Rep.*, 2016, **6**, 32355.
64 T. F. Qahtan, T. O. Owolabi and T. A. Saleh, *J. Mol. Liq.*, 2024, **393**, 123556.

